Sánchez-Arriaga, G., Chen, X., Lorenzini, E.C. (2017). Optimal Design and Deorbiting Performance of Thermionic Tethers in Geostationary Transfer Orbits. *Journal of Propulsion and Power*, 33(2), pp.: 425-432.

DOI: https://doi.org/10.2514/1.B36202

JOURNAL OF PROPULSION AND POWER
Vol. , No. ,

Optimal Design and Deorbiting Performance of Thermionic Tethers in Geostationary Transfer Orbits

G. Sanchez-Arriaga* and X. Chen†
Universidad Carlos III de Madrid, 28911 Leganés, Spain
and
E. C. Lorenzini‡
University of Padova, 35131 Padova, Italy

DOI: 10.2514/1.B36202

The application of a recent concept, a thermionic bare tether (that is, a long conductor coated with a thermionic material), to a practical engineering problem (deorbit space debris from geostationary transfer orbit) is presented. Lorentz drag on a thermionic bare tether, during each pass through an arc close to the perigee, lowers the apogee progressively and produces the object reentry. The performance of a spacecraft equipped with a thermionic bare tether is studied at two different levels, using models that couple thermal and electrical effects. In first place, a simple formula for the eccentricity decrement produced during each perigee pass as a function of TBT properties is derived and used to select TBT optimal dimensions. For a given tether mass, the formula shows that long tethers with small cross-section areas, but large enough to accomplish mechanical constraints, yield the best performance. Second, full numerical simulations of the deorbit maneuver including Lorentz force, air drag, and J_2 perturbations are carried out. A spinning thermionic bare tether with a mass of about 16 kg, as well as a length, width, and thickness equal to 6 km, 2 cm, and 50 μm, respectively, passively deorbits a half-ton spacecraft (with a natural deorbit time of about 50 years) in less than six months, without using propellant, expellant, or power supply. The important roles played by the eclipses and the Earth's oblateness on thermionic bare tether performance are highlighted.

Nomenclature

A	=	tether cross-section area, m^2
$\boldsymbol{B}$	=	geomagnetic field, T
C_D	=	tether drag coefficient
c_t	=	tether specific heat, $J/kg \cdot K$
$\boldsymbol{E}_m$	=	motional electric field, V/m
e	=	eccentricity
$\boldsymbol{F}_{J_2}$	=	J2 perturbation force, N
$\boldsymbol{F}_L$	=	Lorentz force, N
H_p	=	perigee altitude, m
h	=	tether thickness, m
h_p	=	Planck constant, $J \cdot s$
I	=	tether current, A
i	=	inclination, rad
k_B	=	Boltzmann constant, J/K
L	=	tether length, m
m_e	=	electron mass, kg
m_s	=	spacecraft mass, kg
m_t	=	tether mass, kg
N_0	=	plasma density, m^{-3}
p	=	tether perimeter, m
q_e	=	electron charge, c
$\boldsymbol{r}$	=	spacecraft position vector, m
r_p	=	perigee radius, m
S	=	Solar constant, W/m^2
s	=	tether arc-length, m
T	=	tether temperature, K
T_e	=	electron temperature, K
t	=	time, s
t_D	=	deorbit time, s
$\boldsymbol{v}$	=	spacecraft velocity vector, m/s
W	=	work-function, J
w	=	tether width, m
α_{abs}	=	tether absorptivity
β	=	spacecraft frontal area-to-mass ratio
ΔV	=	tether-to-plasma bias, V
ϵ_{em}	=	tether emissivity
μ	=	Earth's gravitational constant, m^3/s^2
ρ_0	=	air density, kg/m^3
σ_B	=	Stefan–Boltzmann constant, $W/m^2 \cdot K^4$
σ_t	=	tether conductivity, $1/\Omega \cdot m$

Received 2 February 2016; revision received 5 July 2016; accepted for publication 25 July 2016; published online XX epubMonth XXXX.

*Ramón y Cajal Research Fellow, Bioengineering and Aerospace Engineering Department, Avda. de la Universidad 30.

†Bioengineering and Aerospace Engineering Department, Avda. de la Universidad 30.

‡Professor, Department of Industrial Engineering; also Member of University Centre of Studies and Activities for Space "Giuseppe Colombo", 35131 Padua, Italy. Senior Member AIAA.

I. Introduction

Objects left in geostationary transfer orbit (GTO), including upper stages, fuel tanks, and payload adapters, periodically cross the two protected regions, i.e., geostationary Earth orbits (GEOs) and low Earth orbits (LEOs). According to the guidelines of the Inter-Agency Space Debris Coordination Committee, their presence shall be limited to a maximum of 25 years. However, an interesting study by Fisher and David [1] showed that the 185 GTO launches during 2004–2012 (210 in total, but 25 without available data) generated 294 mission-related objects in GTO, of which only 43 reentered. The 43 launches of Ariane5 released in GTO 43 upper stages and 40 payload adapters for dual-launch configuration (named SYLDA) [1]. Only five SYLDAs, of which all had low initial perigees (229–268 km), reentered between one and seven years after launch. And, none of the upper stages decayed. These figures were in agreement with theoretical models [2]. Seventy-five of these leftover objects crossed both LEO and GEO, thus posing a threat to operational satellites.

Several measures were taken to deorbit space debris from GTO in less than (or about) 25 years. For instance, although the optimal perigee for Ariane 5 is close to 290 km, Arianespace selected a significantly lower value of 250 km to reduce the lifetime of the upper stage to be only slightly higher than 25 years [2]. This produces a loss of performance: more than 60 kg below the optimum. Ariane 6,

expected in 2021, will incorporate a restartable upper stage that will deorbit in compliance with mitigation guidelines. But, this will not help (in principle) the payload adapter SYLDA. Another mitigation action is a launch planning with favorable sun-synchronous resonance conditions. This can limit the lifetime below 25 years, even for a perigee altitude of about 350 km [3]. Sun-synchronous resonance, which is a result of the interplay of the J2 and the third-body perturbations, increases or decreases the orbit perigee altitude significantly, depending on the orbital elements. However, determining whether an object left in GTO will reenter or not in less than 25 years is difficult because the dynamics is affected by several perturbations. One of the most important (the air drag) that dissipates orbital energy during each pass through the perigee is highly dependent on solar activity. Guidelines will be accomplished confidently if the perigee is placed at 200 km, but this typically penalizes the launcher performance (about 200 kg below optimum for Ariane 5 [2]). As explained in this work, an alternatively effective solution may be the use of a thermionic bare tether (TBT) [4] that can deorbit passively from GTO without propellant, expellant, attitude control, or power supply.

The TBT is the result of more than two decades of intense research on electrodynamic tethers, i.e., long conductors that exchange momentum with the planet magnetosphere. Pioneer electrodynamic tethers in the 1990s, like the Tethered Satellite System-1 and 1R (TSS-1 and TSS-1R) missions, were insulated. They captured electrons from the plasma (anodic contact) using a big conductive sphere and emitted electrons with an electron gun (cathodic contact). A groundbreaking change occurred in 1993, when the bare tether concept was introduced [5]. This type of tether, without insulation, naturally captured electrons as a giant Langmuir probe and achieved cathodic contact with the plasma using an active hollow cathode (HC). The substitution of round bare tethers with tapelike tethers was a second milestone. A tape tether is more robust against cuts by small debris [6] and, for a given mass and length, it collects more current than a round tether due to its larger perimeter.

In 2012, the TBT brought the bare tether concept to its full completion. Instead of using a HC, a TBT is coated with a material of low-work function that emits electrons to the plasma naturally at a relatively low temperature. If the plasma-to-tether bias is large enough, then the thermionic-emission current is limited by temperature effects and follows the Richardson–Dushman law:

$$j_{\mathrm{RD}} = \frac{4\pi m_e q_e k_B^2}{h_p^3} T^2 \exp\left(-\frac{W}{k_B T}\right) \tag{1}$$

where h_p and k_B are Planck and Boltzmann constants, q_e and m_e are the electron charge and mass, T is the temperature of the tether, and W is the work function of the thermionic material. Although HCs are light and used routinely in many space missions, TBTs represent an important progress with respect to bare tethers equipped with HCs. Besides the HC itself, TBT also eliminates the bottle of Xenon (expellant), the flow control unit, and the piping. The TBT is an inert device that works without any active elements and consumables. As shown in this work, their simplicity and robustness make TBTs ideal for deorbiting scenarios.

Important theoretical difficulties arise when describing the current and voltage profiles along a TBT. A complex double layer is formed by the emitted electrons and the collected ions. Kinetic analyses for cylindrical probes in the small-Debye-length ($R \gg \lambda_{\mathrm{DE}}$) [7] and the high-bias ($e|\Delta V|/kT_e \gg 1$) [8] limits were carried out in the past. However, a solid model capturing the full dependence of the emitted current as a function of $R/\lambda_{\mathrm{De}}, T_i/T_e, T/T_e, e\Delta V/kT_e$, and W/kT is not available yet. Here, R is the probe radius, ΔV is the tether-to-plasma bias, λ_{De} is the electron Debye length, and T_e and T_i are the electron and ion temperatures. The seminal work [4], and a later analysis with ohmic effects [9], introduced relatively simple round-tether models that might be accurate enough to find preliminary performance. Our work extends the model in [9] to incorporate thermal effects. Tape geometry is also considered by just setting the tether perimeter accordingly. This was shown to be a good assumption for conventional Langmuir probes [10] but, to the best of our knowledge, the case of an emissive Langmuir probe with tape geometry has not been investigated yet. More elaborated codes, like the one presented in [11], or extensions of the codes in [12–14] to include electron emission could be used in future works to refine this basic model.

This work extends the previous TBT current/voltage profile model to include thermal effects and studies, for the first time, the performance of this device in deorbiting scenarios. Section II explains concisely how to compute the Lorentz force for a TBT and introduces the critical parameters that control its performance (a detailed algorithm to compute tether current and voltage profiles is given in the Appendix). Using a simplified version of the model introduced in Secs. II and III finds a compact formula to estimate TBT performance and selects optimal geometry for a given mission. Numerical simulations of spacecraft dynamics in GTO deorbiting scenarios are presented in Sec. IV, and the conclusions are presented in Sec. V.

II. TBT Model

The most promising thermionic material for TBT applications is the C12A7:e^- electride, which might present a probable work function as low as $W = 0.6$ eV and exceptional stability properties [15]. However, manufacturing effective TBTs has to face at least three important challenges. The first one is to develop an economical process to coat kilometer-long conductive tapes with C12A7:e^-. A good electric contact between the electride and the substrate is also a nontrivial cornerstone. In this respect, a composite of C12A7:e^- and metallic titanium can improve the ohmic contact while keeping the intrinsic work function value of C12A7:e^- [16]. Finally, the properties of the TBT have to be stable under tough space conditions, which include impacts from highly energetic ions along the cathodic segment and the atomic oxygen attack. These are all open issues that require significant research work in material science. Since it is not possible to anticipate the work function of future TBTs, our work assumes a nominal value of $W = 1$ eV and shows how deorbiting performance varies as W is increased. Moreover, tether dimensions can be selected to increase the operational temperature, thus achieving the same electron-emission level while allowing higher work function values (see Sec. III).

A. Dynamical and Thermal Model

We consider a spacecraft orbiting in GTO, equipped with a TBT of mass m_t, perimeter p, cross-section area A, and length L. The TBT-spacecraft system is considered as a rigid dumbbell that spins at a constant rate inside the orbital plane. The coupling that exists between the attitude and the orbital motion of tethered systems in high eccentric orbits [17–19] can be used to build up a spin for stabilizing the system through angular momentum and providing a sufficient tether tension. Here, we are interested in the dynamics of the spacecraft that will be considered as a point mass affected by the gravitational force, the Lorentz force on the TBT $\boldsymbol{F}_L$, the J_2 effect $\boldsymbol{F}_{J_2}$, and the air drag on the TBT–spacecraft system. A self-consistent description of the TBT dynamics is beyond the scope of this work. The dynamics of the spacecraft is governed by

$$\frac{\mathrm{d}^2\boldsymbol{r}}{\mathrm{d}t^2} = -\frac{\mu}{r^3}\boldsymbol{r} - \frac{C_D}{2}\rho_0\left(\beta + \frac{pL}{\pi m_s}\right)v\boldsymbol{v} + \frac{\boldsymbol{F}_{J_2}}{m_s} + \frac{\boldsymbol{F}_L}{m_s} \tag{2}$$

where m_s is the total mass, μ is the Earth standard gravitational parameter, $C_D = 2.2$ is the drag coefficient, ρ_0 is the air density, $\beta = 0.01\ \mathrm{m}^2/\mathrm{kg}$ is the spacecraft frontal-area-to-mass ratio, and $\boldsymbol{v} = \mathrm{d}\boldsymbol{r}/\mathrm{d}t$ is the spacecraft velocity. Our analysis assumes $m_t \ll m_s$ and, for computing the air and Lorentz drags, neglects both the TBT-spin and ionospheric-plasma velocities as compared with $\boldsymbol{v}$.

In preliminary analyses for missions using conventional bare tethers with a HC, tether temperature effects are normally neglected because they just correct tether conductivity σ_t moderately. However, for a TBT, a self-consistent solution of Eq. (2), coupled with the

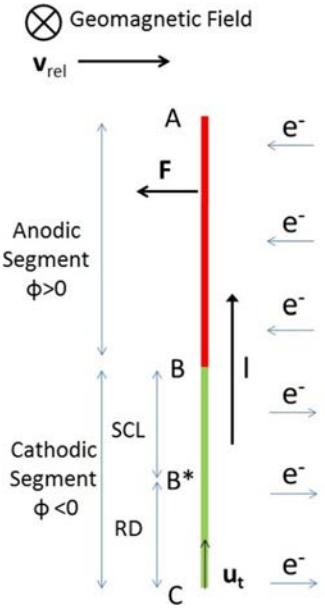

Fig. 1 Operation scheme of the bare-thermionic tether.

evolution of tether temperature T, is essential because, as shown in the following, the emitted current heavily depends on T. A local balance reads [20]

$$\rho A c_t \frac{\mathrm{d}T(s)}{\mathrm{d}t} = \frac{p}{\pi}\left(\alpha_{\mathrm{abs}} S + \frac{C_D}{2}\rho_0 v^3 - \pi\epsilon_{\mathrm{em}}\sigma_B T^4\right) + \frac{I^2}{\sigma_t A} + \dot{W}_e \tag{3}$$

where $\rho = 2700\ \mathrm{kg/m^3}$ and $c_t = 910\ \mathrm{J/kg\cdot K}$ are the tether density and specific heat, respectively; and s is the distance from the anodic end ($0 \le s \le L$, see Fig. 1). This thermal balance, with thermal diffusivity neglected, includes the effects of solar radiation, air drag heating, radiative cooling, ohmic heating, and plasma heating. In our calculations, we use the solar constant $S \approx 1.37\ \mathrm{kW/m^2}$ and the Stefan–Boltzmann constant $\sigma_B \approx 5.67\times10^{-8}\ \mathrm{W/m^2\,K^4}$. Tether absorptivity of $\alpha_{\mathrm{abs}} = 0.5$ and tether emissivity of $\epsilon_{\mathrm{em}} = 0.06$ are chosen according to past tether works [20] and the measurements on Al1100-H19 in the The Bare Electrodynamic Tethers Project (BETs Project) under the EU's Seventh Framework Programme for Research (FP7). The third term in Eq. (3), which involves the current intensity along the tether $I(s)$ and its conductivity $\sigma_t = 3.546\times10^7\ \Omega^{-1}\,\mathrm{m}^{-1}$, is due to Ohmic dissipation. The fourth term is given by

$$\dot{W}_e = \frac{p}{\pi} q_e N_0 \Delta V \sqrt{\frac{2q_e\Delta V}{m_e}} \tag{4}$$

where N_0 is the plasma density. It represents the energy brought up to a tether element by the impact of electrons collected at a tether-to-plasma bias ΔV. This term only applies to the tether anodic segment with $\Delta V > 0$.

B. Lorentz Force

To close Eqs. (2) and (3), it is necessary to find the Lorentz force $\boldsymbol{F}_L$ exerted by the geomagnetic field $\boldsymbol{B}$ on the tether current intensity $\boldsymbol{I}(s) = I(s)\boldsymbol{u}_t$. In this respect, a central role is played by the averaged current intensity

$$I_{\mathrm{av}} = \frac{1}{L}\int_0^L I(s)\,\mathrm{d}s \tag{5}$$

that naturally appears in the Lorentz force as

$$\boldsymbol{F}_L = \int_0^L I(s)\boldsymbol{u}_t \times \boldsymbol{B}\,\mathrm{d}s \equiv L I_{\mathrm{av}}\boldsymbol{u}_t \times \boldsymbol{B} \tag{6}$$

The projection of the motional electric field $\boldsymbol{E} = \boldsymbol{v}\times\boldsymbol{B}$ along the tether is

$$E_m \equiv \boldsymbol{E}_m \cdot \boldsymbol{u}_t = vB\cos\varphi \tag{7}$$

where φ is the angle between $\boldsymbol{B}$ and the unit vector $\boldsymbol{u}_t$, which lies along the straight tether and points in the direction of the tether current (see Fig. 1). Since the TBT is coated entirely with the thermionic material, an electric current circulates independently of the sign of E_m. A thorough explanation about the computation of I_{av} is given in the Appendix. It was an extension of [4] that assumed a constant temperature along the TBT. Now, we discuss briefly the main properties of the dimensionless average current $i_{\mathrm{av}} \equiv I_{\mathrm{av}}/\sigma_t A E_m$ and how it is affected by tether design.

As will be shown in the Appendix, the normalized tether current $i_{\mathrm{av}} = i_{\mathrm{av}}(\xi_C, k_s, k_t)$ depends on three dimensionless parameters. They are the ratios of characteristic lengths that involve TBT design considerations and environmental properties. These three parameters appear naturally when describing the TBT/plasma interaction along the three segments shown in Fig. 1. The dimensionless parameter ξ_C is given by $\xi_C \equiv L/L^*$ with

$$L^* \equiv \left(\frac{2A}{p}\right)^{2/3} \times l_1^{1/3}, \qquad l_1 \equiv \frac{9\pi^2 m_e \sigma_t^2 E_m}{128 q_e^3 N_0^2} \tag{8}$$

and gauges ohmic effects in the anodic segment AB. The cathodic part BC has a segment BB^* where electron emission is space charge limited (SCL). Its physics is controlled by

$$k_s \equiv \frac{l_2}{p}\times\left(\frac{A}{p l_2}\right)^{1/6}, \qquad l_2 \equiv \sqrt{2}\left(\frac{32\pi^2\epsilon_0}{9\sigma_t}\sqrt{\frac{kT_e\sigma_1}{m_e}}\right)^{3/5} l_1^{2/5} \tag{9}$$

with vacuum permittivity ϵ_0 and a constant $\sigma_1 \approx 0.24$ [10,4]. This is a good approximation for preliminary analysis; although, in principle, it is only valid for a tether cross-section characteristic length equal to its maximum for orbital-motion-limited (OML) current collection, i.e., tether radius $R = R_{\max}$ for round tethers and width $w = 4R_{\max}$ for tapes. For certain combinations of ξ_c and k_s, one has $B^* = C$ and the tether is said to operate in the short tether regime. Otherwise, there is a segment B^*C that operates under Richardson–Dushman conditions, governed by the third parameter

$$k_t \equiv \left(\frac{p l_3}{A}\right)^{1/3}, \qquad l_3(\xi) = 4\left[\frac{j_{\mathrm{RD}}}{\sigma_t E_m}\right]^3 l_1 \tag{10}$$

Unlike ξ_C and k_s, the parameter k_t involves tether temperature [see the definition of j_{RD} in Eq. (1)], and thus varies along the tether length.

As shown in Eqs. (8), (9), and (10), under the same environmental conditions, tethers of identical work function, resistivity, and temperature share the same values for l_1, l_2, and l_3. For a tape tether of width w and thickness h, one has $A/p \approx wh/2w = h/2$. Therefore, tape tethers of identical thicknesses and lengths also share the same values for ξ_C and k_t. Parameter k_s depends on the width; higher w yields lower k_s due to the factor l_2/p in Eq. (9). For typical ambient parameters ($N_0 = 3\times10^{11}\ \mathrm{m^{-3}}$, $E_m = 0.15\ \mathrm{V/m}$, $T_e = 0.1\ \mathrm{eV}$), TBT temperature ($T = 500\ \mathrm{K}$), and work function ($W = 1\ \mathrm{eV}$), one finds $k_t \approx 175$ and $\xi_C \approx 6.5$ for a tape TBT of 6 km length and a 50 μm thickness. For different widths, $w = 1, 2$; and 3 cm yields $k_s \approx 5.89$, 2.95, and 1.96, respectively. As compared with round tethers of equal mass and length, where $A/p = R/2$ with R as the tether radius, the tape tethers typically have larger ξ_C and k_t values and smaller k_s values.

Figure 2 shows the normalized average current intensity versus ξ_C for a TBT of constant temperature, with $k_s = 2$, 3, 6 and $k_t = 0.5$, 175. Solid (dashed) lines indicate operation within the short (long)

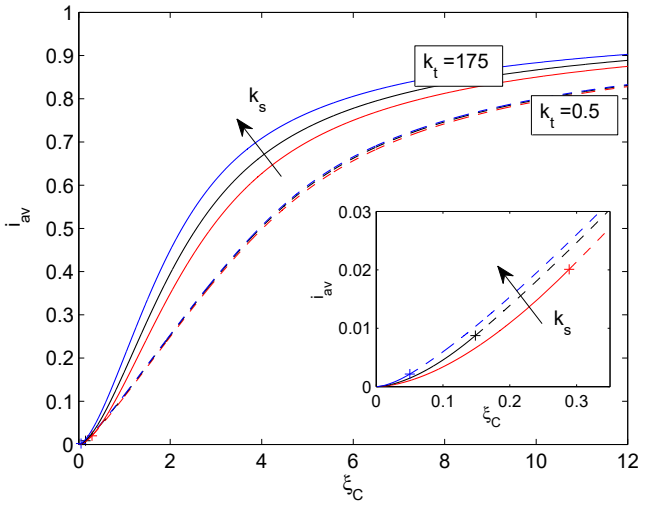

Fig. 2 Normalized average current intensity versus ξ_C, $k_s = 2, 3, 6$; and $k_t = 0.5$ and 175.

tether regime. For $k_t = 175$, the TBT always operates within the short tether regime for all three k_s values. However, for $k_t = 0.5$, a transition to the long tether regime occurs at certain critical ξ_C values, marked with crosses in the inset. These calculations highlight the importance of designing and manufacturing TBTs with large ξ_C, k_s, and k_t values.

III. First Estimation of TBT's Performance

Before running simulations of Eqs. (2) and (3), we first find a simple formula to estimate the performance of a TBT in GTO scenarios. Following [21], the eccentricity decrement per orbit is found. This result can be used for mission design and optimal tether geometry selection. We momentarily ignore air drag and J_2 effects in Eq. (2), and we assume the perigee radius r_p to be constant throughout the deorbit maneuver within the equatorial plane. The eccentricity decrement is then given by [21]

$$\Delta e \approx \frac{2r_p}{\mu}\frac{W_L}{m_s} \tag{11}$$

where W_L is the Lorentz work per orbit, which is effective within an arc close to the perigee because the plasma density and magnetic field are negligible beyond a certain radius: say, $r_{\max}$. In our calculations, we consider a maximum value of $\tilde{r}_{\max} \equiv r/r_p = 1.17$ that corresponds to an altitude of 1400 km. The time elapsed through such an arc, which is about 21 min, is obtained by integrating the relation

$$\frac{\mathrm{d}r}{\mathrm{d}t} = \frac{v_p}{1+e}\sqrt{e^2 - \left(\frac{1+e}{\tilde{r}} - 1\right)^2} \tag{12}$$

which is obtained from the angular momentum conservation $r^2\mathrm{d}\nu/\mathrm{d}t = r_p v_p$ and the orbit equation $1 + e\cos\nu = (1+e)r_p/r$. Here, ν, e, and v_p are the true anomaly, the eccentricity, and the velocity at the perigee, respectively; and we have defined $\tilde{r} \equiv r/r_p$.

Writing the tether mass as $m_t = \rho_t AL$ and using Eqs. (6) and (7), the power dissipated by the Lorentz drag reads

$$\dot{W}_L = \boldsymbol{F}_L \cdot \boldsymbol{v} = -\frac{\sigma_t}{\rho_t} m_t i_{\mathrm{av}} E_m^2 \tag{13}$$

For a high enough spin rate, we can average over angle φ at a fixed spacecraft position and compute the averaged dissipated power as

$$\langle \dot{W}_L \rangle = -\frac{\sigma_t}{\rho_t} m_t B^2 v^2 \langle i_{\mathrm{av}} \cos^2\varphi \rangle \tag{14}$$

The spacecraft velocity in Eq. (14) is given by vis viva equation $v^2 = \mu(2/\tilde{r} - 1 + e)/r_p$. For this simplified model, we will use a dipole magnetic field $B = B_0(R_E/r)^3$, with $B_0 \approx 3.12 \times 10^{-5}$ T and R_E as the Earth radius. Integrating the Lorentz power over the time Δt in the arc close to the perigee, we find the Lorentz work as

$$W_L = \int_{\Delta t} \langle \dot{W}_L \rangle \,\mathrm{d}t = 2\int_{r_p}^{r_{\max}} \frac{\langle \dot{W}_L \rangle \,\mathrm{d}r}{\mathrm{d}r/\mathrm{d}t} \tag{15}$$

Substituting these results into Eq. (11) yields a compact formula for the eccentricity decrement:

$$\Delta e = -\frac{m_t}{m_s}\tilde{B}_0^2 I_0 \tag{16}$$

where

$$\tilde{B}_0^2 \equiv \frac{4\sigma_t B_0^2}{\rho_t}\sqrt{\frac{r_p^3}{\mu}}\left(\frac{R_E}{r_p}\right)^6 \tag{17}$$

is a dimensionless constant, and

$$I_0 \equiv \int_1^{\tilde{r}_{\max}} \frac{\langle i_{\mathrm{av}} \cos^2\varphi \rangle}{\tilde{r}^6} \frac{[2-(1-e)\tilde{r}]\,\mathrm{d}\tilde{r}}{\sqrt{2\tilde{r} - (1-e)\tilde{r}^2 - (1+e)}} \tag{18}$$

The computation of i_{av} in the preceding equation, involving the parameter k_t, requires tether temperature. Instead of solving Eq. (3), we will assume in this section that the TBT is in thermal equilibrium. Then, ignoring the left-hand side of Eq. (3) yields

$$1 - \left(\frac{T(\xi)}{T_0}\right)^4 + \left(\frac{T_1}{T_0}\right)^4 i^2(\xi) = 0 \tag{19}$$

where

$$T_0 = \left[\frac{\alpha_{\mathrm{abs}} S}{\pi \epsilon_{\mathrm{em}} \sigma_B}\left(1 + \frac{C_D \rho_0 v^3}{2\alpha_{\mathrm{abs}} S}\right)\right]^{1/4}, \qquad T_1 = \left(\frac{\sigma_t E_m^2}{\sigma_B \epsilon_{\mathrm{em}}}\frac{A}{p}\right)^{1/4} \tag{20}$$

and $i(\xi)$ and ξ are the normalized current and arc length, respectively [see their definitions in Eq. (A1) of the Appendix].

Equations (11) and (19) are simplified versions of Eqs. (2) and (3). They are coupled because i_{av} depends on tether temperature, which is affected by Joule heating. Each $\tilde{r}$ value in Eq. (18) involves the averaged quantity

$$< i_{\mathrm{av}} \cos^2\varphi > = \frac{2}{\pi}\int_0^{\pi/2} i_{\mathrm{av}} \cos^2\varphi \,\mathrm{d}\varphi \tag{21}$$

where the tether temperature at a given φ is described by Eq. (19).

Figure 3 shows the product $\Delta e \times m_s/m_t$ versus orbit eccentricity for three TBTs of equal mass but different dimensions. Equations (11) and (19) are solved with parameter values $W = 1$ eV and $H_p = 270$ km. It suggests that, for a given mass ratio, a tapelike TBT with a small thickness, small width, and large length is the most effective configuration. A lower bound for the TBT's width and thickness of about 2 cm and 50 μm, respectively, is a reasonable choice to keep a high enough mechanical performance. The tape cross section should be large enough to resist the centrifugal force due to tether spinning. Regarding round TBTs (not shown), the calculation indicates lower performance because, for equal mass, their perimeters are smaller as compared with tapelike configurations. They present lower values for the collected and emitted currents, thus yielding lower values for eccentricity decrement per orbit revolution.

Optimum TBT geometry selection in GTO is not obvious. In LEO, tether cut probability by small debris poses a constraint that can be used to find an optimum [22]. However, tether cut failure does not

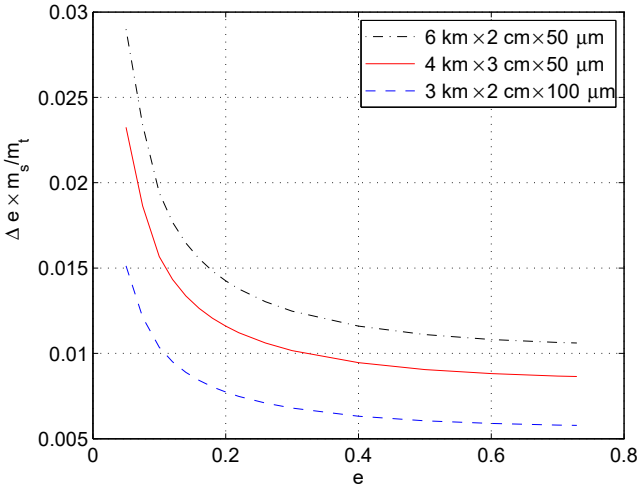

Fig. 3 Eccentricity decrement by mass ratio product versus orbit eccentricity.

seem to be troublesome in GTO, where the space debris flux is very low during most of the time along one orbit revolution. To find optimal geometry in GTO, a maximum upper bound for the deorbit time t_D may come from guidelines or international regulations. However, as shown in Sec. IV, the actual 25-year rule is too weak for TBTs, which can deorbit more than one order of magnitude faster by using a low m_t/m_s ratio. An alternative reason to impose a maximum t_D value is the possible degradation of the thermionic coating, i.e., W increasing with time due to the tough space environment. Unfortunately, TBTs have not been manufactured yet and it is not possible to anticipate whether this issue will be important or not. For these reasons, the next section shows detailed dynamical simulations where no coating degradation happens but missions are designed to deorbit the spacecraft in less than one year.

IV. Mission Performance

Tether flight simulator BETsMA [23], which integrates Eq. (2), was updated to incorporate the TBT current and voltage profiles given in the Appendix and the time-dependent temperature profile described by Eq. (3). The code computes the temperature evolution of 20 points along the TBT. The tether is taken as a dumbbell straight bar that spins within the orbital plane at a constant rate of 0.5 rpm. The geomagnetic field, electron plasma density and temperature, and air density are computed by the code with the International Geomagnetic Reference Field, the 2012 International Reference Ionosphere, and the COSPAR International Reference Atmosphere (CIRA) model under moderate solar activity, respectively. BETsMA takes into account the relative position between the Earth and the sun, and it sets $S = 0$ in Eq. (3) when the spacecraft is inside the Earth's shadow. The code estimates the tether cut probability during the deorbiting maneuver. It computes the number of fatal impacts by small debris using the algorithm from [6]. For an altitude less than 1500 km, the debris flux is computed from a database obtained from the ESA Meteoroid and Space Debris Terrestrial Environment (MASTER) model, whereas for higher altitudes, BETsMA implements the Grün's micrometeoroid model. As initial conditions, we took a 500 kg spacecraft, with a TBT on board, in a GTO ($i = 6$ deg, $e = 0.729$, $H_p = 270$ km) on 1 January 2004. Other tether values, like density and conductivity, were equal to the ones given in Sec. II. The coating work function was 1 eV and, according to the analysis in Sec. III, the tape dimensions were set to $L = 6$ km, $w = 2$ cm, and $h = 50$ μm. Our simple analytical models, like Eqs. (16) and (19), were used to check the correct implementation of the code.

We first look at the thermal and electrical behavior of a TBT during the first orbit revolution. Figure 4 shows the evolution of $i_{\rm av}$ and the temperature at the half-tether length versus the true anomaly. Away from the perigee, the current intensity vanishes, due to the low plasma density, and the tether temperature is almost constant, being $T_0 \approx$

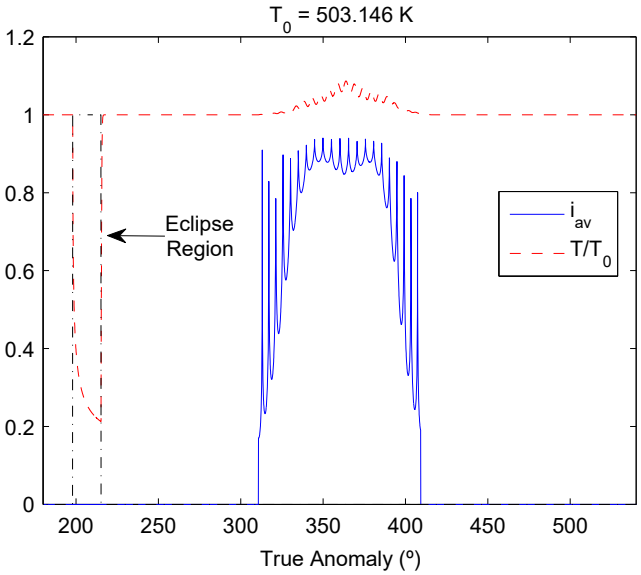

Fig. 4 Tether temperature and $i_{\rm av}$ versus true anomaly.

503 K [see Eq. (20)]. Close to the perigee, where plasma density is important, a current circulates along the TBT that becomes hotter due to the ohmic heating. The oscillations exhibited by $i_{\rm av}$ in Fig. 4 are due to the spinning motion. High efficiencies, with $i_{\rm av} \approx 0.9$, can be achieved. For this almost equatorial orbit, the current intensity is maximum when the tether is aligned with the local vertical at the perigee, where the motional electric field reaches a value close to 330 V/km. Another important feature is the role played by the relative positions of the sun, the Earth, and the TBT. At each time that the spacecraft enters inside the Earth's shadow, marked with dashed black lines in Fig. 4, the tether temperature decreases abruptly (see Fig. 4 with true anomaly close to 200 deg). It increases rapidly as soon as the sun illuminates it again. Therefore, tether deployment has to be planned to place the perigee outside the Earth's shadow. Otherwise, the tether will be cold at the perigee and thermionic emission will not be efficient. It will be shown later that J_2 perturbation is beneficial by avoiding configurations with the perigee inside the Earth shadow during a long period of time.

Figure 5 displays the relative lengths of the anodic (L_B/L) and cathodic ($L_{\rm BC}/L$) tether segments and the normalized electron plasma density versus altitude during one half-orbit revolution. In this particular case, the full $L_{\rm BC}$ segment works under SCL

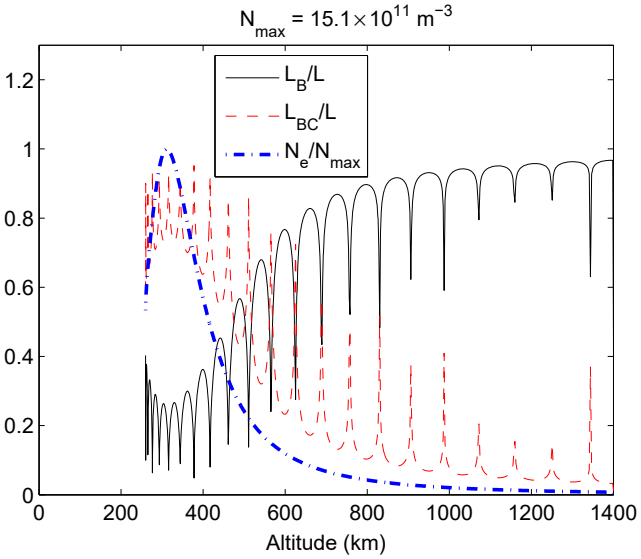

Fig. 5 Normalized electron density ($N_e/N_{\rm max}$), as well as anodic (L_B/L) and cathodic ($L_{\rm BC}/L$) segments versus orbit altitude.

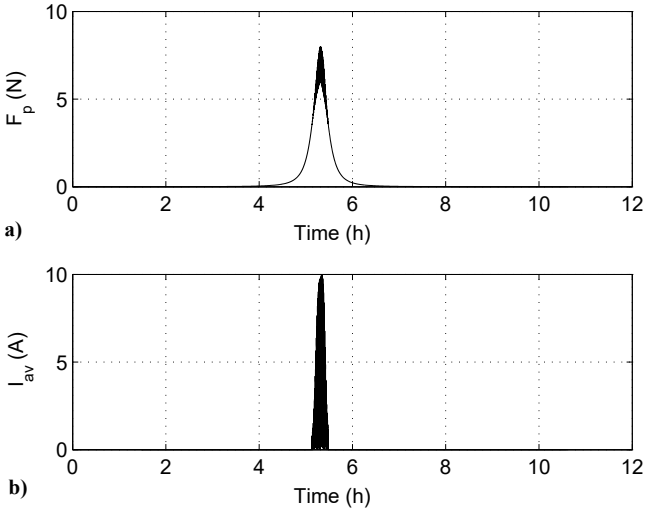

Fig. 6 Representations of a) perturbation force and b) averaged current intensity versus time.

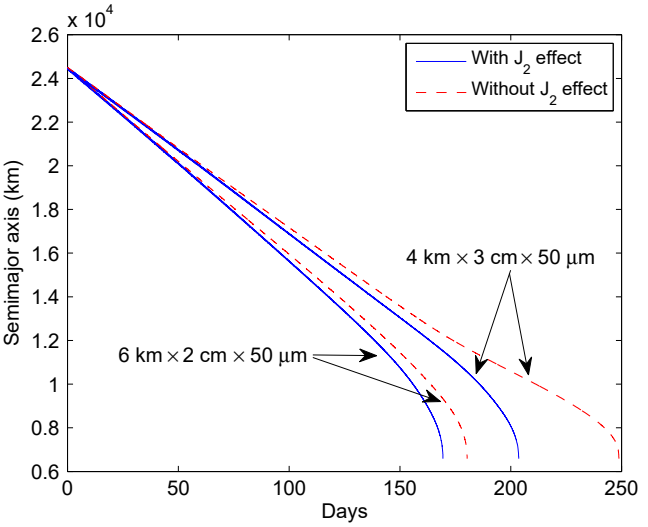

Fig. 7 J_2 effect impact on deorbit time for two tether geometries.

conditions (short tether regime). Close to the perigee, where plasma density is high, the OML current collection is very efficient and the anodic segment is less than 40% of the full tether length. For an altitude between 550 and 650 km, with plasma density in the range of $2–5 \times 10^{11}$ m^{-3}, anodic and cathodic-segment lengths are similar. Above 800 km of altitude, thermionic emission is much more efficient than electron current collection due to the low plasma density, and most of the tether length acts as a giant collecting Langmuir probe. The periodic behavior exhibited by the lengths of the anodic and cathodic segments (period equal to 1 min) is a direct consequence of the 0.5 rpm spinning velocity of the TBT.

Figure 6a shows the evolution of the modulus of the resultant of the perturbation forces during one orbit revolution. The maximum values of the J_2 effect, the Lorentz force, and the aerodynamic drag are about 6.5, 2, and 0.6 N, respectively. Although the J_2 force is the largest, this effect does not produce a variation of the semimajor axis over a complete revolution. Only the Lorentz and aerodynamic drags contribute directly to the spacecraft deorbiting. As shown in Fig. 6b, the maximum average current intensity along the TBT through the perigee pass can reach values close to 10 A. If the spacecraft is placed at an intermediate point on the TBT, then this current intensity can be used to feed an interposed load and to generate power for onboard use.

We now discuss the performance of the system during a full deorbit maneuver. First, we integrated Eq. (2) without a TBT under the same initial conditions ($i = 6$ deg, $e = 0.729$, $H_p = 270$ km). The simulation showed that the aerodynamic drag acting on the spacecraft needed about 50 years to complete the deorbiting maneuver. The second simulation with a TBT of dimensions of 6 km × 2 cm × 50 μm, but switching off the Lorentz drag, yielded a deorbit time of $t_D = 3.17$ years. This was equivalent to the use of a drag augmentation device, like a sail or a balloon, with an area of about $L \times w = 120$ m^2. The third simulation with the Lorentz force activated gave $t_D \approx 170$ days. Therefore, adding a TBT of 16.2 kg, below 3.25% of the spacecraft mass, reduced the deorbit time from 50 years to less than six months.

As discussed in Sec. III, TBT geometry selection is important to achieve good performance. For instance, keeping the TBT mass equal to 16.2 kg, but now taking the dimensions as 4 km × 3 cm × 50 μm and 3 km × 2 cm × 100 μm, yields $t_D = 203$ and 333 days, respectively. The role played by the work function is even more dramatic. For a 6 km × 2 cm × 50 μm TBT with $W = 1.3$ eV and 1.4 eV, one finds $t_D = 233$ and 684 days, respectively.

As shown in Fig. 7, although the J_2 effect does not produce secular variation of the semimajor axis, it influences the performance notably through secular variations of perigee argument. For given tether dimensions, we find that the J_2 effect typically helps to produce faster deorbiting maneuvers. In simulations without the J_2 effect, we observe that the perigee of the orbit can spend long periods inside the Earth's shadow. At this configuration, the TBT is almost ineffective because it becomes cold and the plasma density is smaller than in the day side. The secular perigee drift produced by the J_2 effect is very helpful for mitigating this unfavorable configuration.

V. Conclusions

This work shows that a spinning TBT, with dimensions of 6 km × 2 cm × 50 μm, deorbits a spacecraft of mass 500 kg in less than six months without using propellant, expellant, or power supply. The simulations indicate that this deorbit time is two orders of magnitude smaller than its natural decay time and seven times faster than the one given by a drag augmentation device with the same area as the TBT. The very small TBT-to-spacecraft mass ratio, which is about 0.032, shows that adding this passive deorbit technology will have a low impact on launcher performance.

Long tethers with a small cross-section area, which has a lower bound due to mechanical considerations, are the most effective choice. Besides its geometry, tether optical properties also play a very important role. The values used in this work ($\epsilon_{em} = 0.06$ and $\alpha_{abs} = 0.5$) yield a tether temperature close to 500 K throughout most of the GTO. The tether temperature increases about 10% during the perigee pass due to ohmic heating effects. Therefore, for the work function value used, no active means are necessary to keep the tether temperature high enough to make thermionic emission effective. As shown by the simulations, it is essential to describe self-consistently the thermal and the electrical behaviors of the TBT and to include eclipse and J_2 effects. In this respect, deorbit missions have to be designed to avoid placing the GTO perigee inside the Earth's shadow.

Its fully passive character and the absence of propellant and expellant suggest that a TBT can be a very reliable device. However, there are three critical issues related with risk analysis: 1) a possible failure during tether deployment, 2) the tether cut by small debris, and 3) degradation of the thermionic coating. Regarding tether cut, the total number of fatal impacts given by BETsMA in a deorbiting mission with a 6 km × 2 cm × 50 μm tether is $N_c = 4.0 \times 10^{-3}$, thus showing that tether sever probability may not be troublesome in GTO scenarios. In the situation where the thermionic coating will be degraded and the Lorentz drag is not efficient beyond a certain time, the aerodynamic drag on the TBT and the spacecraft will complete the deorbit maneuver in less than 3.2 years in the worst scenario (TBT degradation soon after deployment). This t_D is well below the 25-year guideline and shows a very low risk of implementing TBT missions.

A particular feature that distinguishes electrodynamic tethers from other devices is their capability to probe space plasmas and obtain interesting scientific data. This could change the actual view of deorbiting technologies, which are now perceived by space

companies as a cost that increases the launcher mass. A light deorbit kit based on TBT technology equipped with some simple instruments can be doubly beneficial. For instance, theoretical models of current collection and emission by conductors immersed in plasmas could be tested, and active experiments on nonlinear plasma waves can be carried out while deorbiting. The extra mass added to the deorbit kit, which would slightly penalize its mass and simplicity, could be largely compensated by the obtained scientific information.

Appendix A: TBT Current and Voltage Profiles

This Appendix discusses the computation of the average current $I_{\rm av}$ in Eq. (6). It extends [9] to include the temperature variation along the TBT. For convenience, we will use the normalized variables

$$\xi \equiv \frac{s}{L^*}, \qquad i \equiv \frac{I}{\sigma_t A E_m}, \qquad \phi \equiv \frac{\Delta V}{E_m L^*} \tag{A1}$$

where

$$L^* \equiv l_1^{1/3} \times \left(\frac{2A}{p}\right)^{2/3} \tag{A2}$$

is a characteristic length that gauges ohmic effects.

In a frame attached to the tether, there is a motional electric field $\boldsymbol{E}_m = \boldsymbol{v} \times \boldsymbol{B}$ in the highly conductive ambient plasma. The projection of $\boldsymbol{E}_m$ along the straight tether, given by Eq. (7), will drive a current intensity $\boldsymbol{I} = I(s)\boldsymbol{u}_t$ inside the tether with $\boldsymbol{I} \cdot \boldsymbol{E}_m > 0$. A normalized tether-to-plasma bias profile is governed by [5]

$$\frac{{\rm d}\phi}{{\rm d}\xi} = i - 1 \qquad 0 \le \xi \le \xi_C \equiv L/L^* \tag{A3}$$

Regarding current profile, there is a tether segment with $\Delta\phi > 0$ that captures electrons as a giant Langmuir probe (see Fig. 1). Assuming a high-bias orbital-motion-limited regime, one has

$$\frac{{\rm d}i}{{\rm d}\xi} = \frac{3}{4}\phi^{1/2}, \qquad 0 \le \xi < \xi_B \tag{A4}$$

where ξ_B is the zero-biased point with $\phi(\xi_B) \equiv \phi_B = 0$. The integration of Eqs. (A3) and (A4) with the boundary conditions $i(0) = 0$ and $\phi(\xi_B) = 0$ yields [A1]

$$\phi(i) = (i_B - i)^{2/3}(2 - i_B - i)^{2/3} \tag{A5}$$

$$i(v) = 1 - (1 - i_B)\cosh v \tag{A6}$$

$$\xi(v) = \frac{4}{3}(1 - i_B)^{1/3}[f(v_0) - f(v)] \tag{A7}$$

with $i_B \equiv i(\xi_B)$ and

$$f(x) = \int_0^x \sinh^{1/3}\zeta \, {\rm d}\zeta, \qquad v_0 \equiv a\cosh\left(\frac{1}{1 - i_B}\right) \tag{A8}$$

The auxiliary variable v takes values v_0 and zero at points A and B, respectively. From Eq. (A7), one finds the length of the anodic segment as a function of i_B as

$$\xi_B \equiv \xi(v = 0) = \frac{4}{3}(1 - i_B)^{1/3} f(v_0) \tag{A9}$$

and, from Eq. (A5), the bias at point A as $\phi_A \equiv \phi(0) = [1 - (1 - i_B)^2]^{2/3}$.

The complementary segment BC has $\phi < 0$ and emits electrons thanks to the thermionic coating. However, close to point B, the tether cannot emit the full Richardson–Dushman (RD) current due to space-charge-limited effects [A2]. The current profile within this segment is described by [9]

$$\frac{{\rm d}i}{{\rm d}\xi} = k_s^2\phi, \qquad \xi_B \le \xi < \xi_B \tag{A10}$$

The integration of Eqs. (A3) and (A10) with $\phi(\xi_B) = 0$ and $i(\xi_B) = i_b$ yields

$$\phi(\xi) = -\frac{(1 - i_B)}{k_s}\sinh[k_s(\xi - \xi_B)] \tag{A11}$$

$$i(\xi) = 1 - (1 - i_B)\cosh[k_s(\xi - \xi_B)] \tag{A12}$$

Condition $i(\xi_C) = 0$ in Eq. (A12) yields the following equation for i_B:

$$F_{\rm short}(i_B) \equiv 1 - (1 - i_B)\cosh[k_s(\xi_C - \xi_B)] = 0 \tag{A13}$$

with ξ_B given by Eq. (A9). This TBT configuration, where the full cathodic segment operates under SCL conditions, is called the short tether regime. In this case, the potential at point C is $\phi_C = -\phi_A^{3/4}/k_s$.

As shown in [4], in the long tether regimes, the cathodic-segment emission switches from SCL current to RD current at point B^*. This is the case shown in Fig. 1, where the RD segment is governed by

$$\frac{{\rm d}i}{{\rm d}\xi} = -k_t(\xi), \qquad \xi_{B^*} \le \xi < \xi_C \tag{A14}$$

A good approximation to determine point B^* is found by equalizing the right-hand sides of Eqs. (A10) and (A14). This approximation gives $\phi_{B^*} = -k_t(\xi_{B^*})/k_s^2$ that, after substituting in Eqs. (A11) and (A12), yields

$$\xi_{B^*} = \xi_B + \frac{1}{k_s}{\rm arcsinh}\left[\frac{k_t \xi B*}{k_s(1 - i_B)}\right] \tag{A15}$$

$$i_{B^*} = 1 - \sqrt{(1 - i_B)^2 + (k_t(\xi_{B^*})/k_s)^2} \tag{A16}$$

Current and voltage profiles in segment $\xi_{B^*} \le \xi \le \xi_C$ are obtained by solving Eqs. (A3) and (A14), giving

$$i(\xi) = \int_\xi^{\xi_C} k_t(s)\,{\rm d}s \equiv g(\xi) \tag{A17}$$

$$\phi(\zeta) = -\frac{k_t(\xi_{B^*})}{k_s^2} - (\xi - \xi_{B^*}) + \int_{\xi_{B^*}}^{\xi} g(s)\,{\rm d}s \tag{A18}$$

Condition $i(\xi_{B^*}) = i_{B^*}$ provides an equation for i_B in the long tether regime:

$$F_{\rm long}(i_B) \equiv 1 - \sqrt{(1 - i_B)^2 + (k_t(\xi_{B^*})/k_s)^2} - g(\xi_{B^*}) = 0 \tag{A19}$$

and the cathode bias is

$$\phi_C = -\frac{k_t(\xi_{B^*})}{k_s^2} - (\xi - \xi_{B^*}) + \int_{\xi_{B^*}}^{\xi_C} g(s)\,{\rm d}s \tag{A20}$$

Throughout the numerical integration of Eqs. (2) and (3), the Lorentz force and i_{av} should be computed at each time step. The latter is found from

$$i_{\mathrm{av}} = \frac{1}{\xi_C}\int_0^{\xi_C} i(\xi)\,\mathrm{d}\xi = 1 - \frac{1}{\xi_C}(\phi_A - \phi_C) \tag{A21}$$

where we use Eq. (A3). Given tether parameters, temperature distribution $T(s)$, and environmental parameters (plasma properties and geomagnetic field), the values for ξ_C, k_s, and $k_t(\xi)$ are found. Then, an initial guess of i_B is corrected following a Newton method that involves two steps. First, the operation regime is determined. The values of ξ_B and ξ_{B^*} are found from Eqs. (30) and (36). The latter is a nonlinear equation that should be solved numerically with an inner Newton method. If $\xi_{B^*} > \xi_C$, then the tether operates within the short tether regime and the algorithm goes to the second step. If $\xi_{B^*} < \xi_C$, then $\phi_{B^*} = -k_t(\xi_{B^*})/k_s^2$ and ϕ_C is computed from Eq. (A20). The tether operates within the short (long) regime if $\phi_C > \phi_{B^*}$ ($\phi_C < \phi_{B^*}$). Once the regime is determined, the algorithm implements step 2, where the value of i_B is updated according to

$$i_B \to i_B - \frac{F(i_B)}{\mathrm{d}F/\mathrm{d}i_B|_{i_B}} \tag{A22}$$

Here, F is equal to F_{short} or F_{long}, depending on the regime found by step 1. The procedure is repeated until the error is below a certain prescribed tolerance ($|F(i_B)| < 10^{-12}$ in our simulations).

Acknowledgment

This work was supported by the Ministerio de Economía y Competitividad of Spain (grant no. RYC-2014-15357)

References

[1] Fisher, S., and David, E., "Debris Creation in Geostationary Transfer Orbits: A Review of Launch Practices 2004-2012," *65th International Astronautical Congress*, IAF Paper IAC-14-A6.4.7, Toronto, Canada, 2014, pp. 1–10.

[2] Bonnal, C., Gigou, J., and Aubin, D., "Space Debris Mitigation Measures Applied to European Launchers," *Acta Astronautica*, Vol. 65, Nos. 11–12, Dec. 2009, pp. 1679–1688. doi:10.1016/j.actaastro.2009.04.021

[3] Johnson, N. L., "Space Debris Mitigation Strategies and Practices in Geosynchronous Transfer Orbits," *Advances in Space Research*, Vol. 35, No. 7, 2005, pp. 1328–1334. doi:10.1016/j.asr.2004.11.037

[4] Williams, J. D., Sanmartin, J. R., and Rand, L. P., "Low Work-Function Coating for an Entirely Propellantless Bare Electrodynamic Tether," *IEEE Transactions on Plasma Science*, Vol. 40, No. 5, May 2012, pp. 1441–1445. doi:10.1109/TPS.2012.2189589

[5] Sanmartin, J. R., Martinez-Sanchez, M., and Ahedo, E., "Bare Wire Anodes for Electrodynamic Tethers," *Journal of Propulsion and Power*, Vol. 9, No. 3, 1993, pp. 353–360. doi:10.2514/3.23629

[6] Khan, S. B., and Sanmartin, J. R., "Survival Probability of Round and Tape Tethers Against Debris Impact," *Journal of Spacecraft and Rockets*, Vol. 50, No. 3, May 2013, pp. 603–608. doi:10.2514/1.A32383

[7] Chang, K. W., and Bienkowski, G. K., "Effects of Electron Emission on Electrostatic Probes at Arbitrary Pressures," *Physics of Fluids*, Vol. 13, No. 4, 1970, Paper 902. doi:10.1063/1.1693032

[8] Chen, X., and Sanmartín, J. R., "Low Work-Function Thermionic Emission and Orbital-Motion-Limited Ion Collection at Bare-Tether Cathodic Contact," *Physics of Plasmas*, Vol. 22, No. 5, 2015, Paper 053504.

[9] Chen, X., and Sanmartn, J. R., "Bare-Tether Cathodic Contact Through Thermionic Emission by Low-Work-Function Materials," *Physics of Plasmas*, Vol. 19, No. 7, July 2012, Paper 073508. doi:10.1063/1.4736987

[10] Sanmartn, J. R., and Estes, R. D., "The Orbital-Motion-Limited Regime of Cylindrical Langmuir Probes," *Physics of Plasmas*, Vol. 6, No. 1, Jan. 1999, pp. 395–405. doi:10.1063/1.873293

[11] Chen, X., "Low-Work-Function Thermionic Emission and Orbital-Motion-Limited Ion Collection at Bare-Tether Cathodic Contact," Ph.D. Dissertation, Univ. Politécnica de Madrid, Madrid, Spain, 2015.

[12] Choiniere, E., "Theory and Experimental Evaluation of a Consistent Steady-State Kinetic Model for Two-Dimensional Conductive Structures in Ionospheric Plasmas with Application to Bare Electrodynamic Tethers in Space," Ph.D. Dissertation, Univ. of Michigan, Ann Arbor, MI, 2004.

[13] Sánchez-Arriaga, G., "A Direct Vlasov Code to Study the Non-Stationary Current Collection by a Cylindrical Langmuir Probe," *Physics of Plasmas*, Vol. 20, No. 1, Jan. 2013, Paper 013504. doi:10.1063/1.4774398

[14] Sánchez-Arriaga, G., and Pastor-Moreno, D., "Direct Vlasov Simulations of Electron-Attracting Cylindrical Langmuir Probes in Flowing Plasmas," *Physics of Plasmas*, Vol. 21, No. 7, July 2014, Paper 073504. doi:10.1063/1.4889732

[15] Toda, Y., Matsuishi, S., Hayashi, K., Ueda, K., Kamiya, T., Hirano, M., and Hosono, H., "Field Emission of Electron Anions Clathrated in Subnanometer-Sized Cages in $[Ca24Al28O64]^{4+}(4e^-)$", *Advanced Materials*, Vol. 16, No. 8, 2004, pp. 685–689. doi:10.1002/(ISSN)1521-4095

[16] Yoshizumi, T., and Hayashi, K., "Thermionic Electron Emission from a Mayenite Electride-Metallic Titanium Composite Cathode," *Applied Physics Express*, Vol. 6, No. 1, Jan. 2013, Paper 015802. doi:10.7567/APEX.6.015802

[17] Swan, P., *Dynamics and Control of Tethers in Elliptical Orbits*, Ph.D Dissertation, Univ. of California, Los Angeles, CA, 1984.

[18] Pelaez, J., and Andres, Y. N., "Dynamic Stability of Electrodynamic Tethers in Inclined Elliptical Orbits," *Journal of Guidance, Control, and Dynamics*, Vol. 28, No. 4, 2005, pp. 611–622. doi:10.2514/1.6685

[19] Fujii, H. A., Ichiki, W., Suda, S., and Watanabe, T., "Chaos Analysis on Librational Control of Gravity-Gradient Satellite in Elliptic Orbit," *Journal of Guidance, Control, and Dynamics*, Vol. 23, No. 1, 2000, pp. 145–146. doi:10.2514/2.4500

[20] Sanmartin, J. R., Lorenzini, E. C., and Martinez-Sanchez, M., "Electrodynamic Tether Applications and Constraints," *Journal of Spacecraft and Rockets*, Vol. 47, No. 3, May 2010, pp. 442–456. doi:10.2514/1.45352

[21] Charro, M., Sanmartin, J. R., Bombardelli, C., Sanchez-Torres, A., Lorenzini, E. C., Garrett, H. B., and Evans, R. W., "A Proposed Two-Stage Two-Tether Scientific Mission at Jupiter," *IEEE Transactions on Plasma Science*, Vol. 40, No. 2, Feb. 2012, pp. 274–281. doi:10.1109/TPS.2011.2172637

[22] Sanmartin, J. R., Sanchez-Torres, A., Khan, S. B., Sanchez-Arriaga, G., and Charro, M., "Optimum Sizing of Bare-Tape Tethers for De-Orbiting Satellites at End of Mission," *Advances in Space Research*, Vol. 56, No. 7, Oct. 2015, pp. 1485–1492.

[23] Sánchez-Arriaga, G., Bombardelli, C., and Chen, X., "Impact of Nonideal Effects on Bare Electrodynamic Tether Performance," *Journal of Propulsion and Power*, Vol. 31, No. 3, 2015, pp. 951–955. doi:10.2514/1.B35393

[A1] Sanjurjo, M., Sanchez-Arriaga, G., and Pelaez, J., "Efficient Computation of Current Collection in Bare Electrodynamic Tethers in and Beyond OML Regime," *Journal of Aerospace Engineering*, Vol. 28, No. 6, Nov. 2014, Paper 04014144.

[A2] Langmuir, I., "The Effect of Space Charge and Residual Gases on Thermionic Currents in High Vacuum," *Physical Review*, Vol. 2, No. 6, Dec. 1913, pp. 450–486. doi:10.1103/PhysRev.2.450

Dr. G. G. Spanjers
Associate Editor